



Deposited via The University of Leeds.

White Rose Research Online URL for this paper:

<https://eprints.whiterose.ac.uk/id/eprint/222859/>

Version: Accepted Version

Article:

Guo, C., Bi, C., Wei, S. et al. (2025) Highly Efficient and Stable CsPbI₃ Perovskite Quantum Dots Light-Emitting Diodes Through Synergistic Effect of Halide-Rich Modulation and Lattice Repair. *Small*, 21 (8). 2409630. ISSN: 1613-6810

<https://doi.org/10.1002/sml.202409630>

This is an author produced version of an article published in *Small*, made available under the terms of the Creative Commons Attribution License (CC-BY), which permits unrestricted use, distribution and reproduction in any medium, provided the original work is properly cited.

Reuse

This article is distributed under the terms of the Creative Commons Attribution (CC BY) licence. This licence allows you to distribute, remix, tweak, and build upon the work, even commercially, as long as you credit the authors for the original work. More information and the full terms of the licence here:

<https://creativecommons.org/licenses/>

Takedown

If you consider content in White Rose Research Online to be in breach of UK law, please notify us by emailing eprints@whiterose.ac.uk including the URL of the record and the reason for the withdrawal request.

Highly Efficient and Stable CsPbI₃ Perovskite Quantum Dots Light-Emitting Diodes through Synergistic Effect of Halide-rich Modulation and Lattice Repair

Chiyu Guo[†], Chenghao Bi^{†}, Shibo Wei, Ke Ren, Xuexuan Huang, Liang Tao, Xingyu Wang, Nora H. de Leeuw, Wenxin Wang**

C. Guo, C. Bi, S. Wei, K. Ren, X. Huang, L. Tao, W. Wang
College of Physics and Optoelectronic Engineering, Harbin Engineering University, Harbin 150001, China.
Qingdao Innovation and Development Base, Harbin Engineering University, Qingdao 266000, China.

E-mail: chenghao.bi@hrbeu.edu.cn; wenxin.wang@hrbeu.edu.cn.

C. Bi
Yantai Research Institute, Harbin Engineering University, Yantai 264000, P.R. China

X. Wang, N. H. de Leeuw
School of Chemistry, University of Leeds, Leeds LS2 9JT, UK.
Department of Earth Sciences, Utrecht University, 3584 CB Utrecht, The Netherlands.

ORCID

Chenghao Bi: 0000-0002-6074-1412
Manling Sui: 0000-0002-0415-5881
Wenxin Wang: 0000-0001-8191-3976

Keywords: perovskite quantum dots, halide-rich environment, lattice repair, PeLEDs, stability

Currently, CsPbI₃ quantum dots (QDs) based light-emitting diodes (LEDs) are not well suited for achieving high efficiency and operational stability due to the binary-precursor method and purification process, which often results in the nonstoichiometric ratio of Cs/Pb/I. This imbalance leads to amounts of iodine vacancies, inducing severe non-radiative recombination processes and phase transitions of QDs. Herein, we report red-emitting CsPbI₃ QDs with excellent optoelectronic properties and stability based on the synergistic effects of halide-rich modulation passivation and lattice repair. Firstly, a ternary-precursor method is employed to better control the feed ratio of Cs/Pb/I and create a halide-rich environment. Secondly, a solvent-free solid-liquid reaction employing a multifunctional guanidinium iodide (GAI) additive was used after purification to repair iodine vacancies and partially replace surface Cs atoms, thereby effectively modifying its tolerance factor. Additionally, these short-chain GA⁺ can be used as the surface ligand to improve the conductivity of the QDs and suppress trap-assisted non-radiative Auger recombination. Consequently, PeLEDs based on GAI-QDs exhibit a great maximum external quantum efficiency (EQE) of 27.1% and an operational half-lifetime (T₅₀) of 1001.1 min at an initial luminance of 100 cd/m².

1. Introduction

Metal halide perovskite quantum dots (QDs), such as CsPbX₃ (X = Cl, Br, I), have gained considerable attention due to their bright and narrow-band light emission in the visible and near-infrared spectra, as well as a maximum photoluminescence quantum yield (PLQY) of up to 100%, exhibit excellent chemical properties. In addition, the stringent fabrication conditions associated with conventional III-V inorganic semiconductor materials and the limited stability of OLEDs have driven extensive research and development of high-efficiency light-emitting diodes (LEDs)^[1]. LEDs based on perovskite QDs (PeLEDs) have attracted more attention due to significant efficiency improvements. Red, green and blue-emitting PeLEDs exhibit excellent external quantum efficiency (EQE) exceeding 20%^[2]. In contrast to conventional organic-inorganic perovskites, all-inorganic perovskites show enhanced stability. And CsPbI₃ QDs show an intrinsic bandgap of 1.73 eV, their PL peak can be adjusted from orange to deep red by changing the size of QDs based on quantum confinement effect. However, the lower formation energy of vacancies in CsPbI₃ renders it more susceptible to phase transitions, a critical challenge requiring immediate attention. This work focuses on mitigating crystal phase distortions and increasing the vacancy formation energy.

However, CsPbI₃ QDs, which is the main emitting layer of deep-red PeLEDs, are susceptible to phase transformation from the initially stable black phase (α cubic phase) to the non-fluorescent yellow phase (δ orthorhombic phase) under external environmental influences^[3]. This instability arises from the fact that the tolerance factor of CsPbI₃ falls within the approximate range of 0.8-1. Relevant calculation formula can be found in the **Supporting Information** of the calculation of the tolerance factor. Under these environment, the tolerance factor of the Cs ion is insufficient to maintain a cubic perovskite structure at room temperature^[4]. Moreover, the most prevalent synthesis method for CsPbI₃ currently is the binary-precursor hot-injection method^[1k]. This method employs PbI₂ as the precursor for lead cations and halide anions, leading to a fixed stoichiometric ratio of 1:2 between the two elements. This results in a significant number of iodine vacancies, which makes the QDs more susceptible to phase transformation and significantly impacts their stability and optical properties. Furthermore, the synthesis process often generates by-products, significantly impacting the experimental yield. To minimize the amount of by-products, an excess of PbI₂ is typically used, which increases production cost^[5]. Current optimization strategies primarily involve supplementing halide vacancies by adding metal halides such as KI or MnI₂ during the reaction process^[6]. Shen et al. synthesized CsPb_{0.64}Zn_{0.36}I₃ by doping with a certain proportion of ZnI₂ during the reaction, resulting in improved optical properties and stability. However, the resulting PeLEDs show a brightness of 2202 cd/m² and an EQE of only 15.1%^[7]. It is attributed to the limited solubility of metal halides in ODE, leading to the insufficient passivation of halide vacancies and waste of significant material^[8]. Furthermore, a small amount of iodide ions may detach along with the surface ligands during long-term storage, resulting in a stoichiometric ratio of Pb and I less than 1:3, leading to a decrease in PLQY and stability^[1d, 9]. Therefore, a method for separately preparing Cs, Pb, and I precursors is proposed by Imran et al. to allow more rational adjustment of the proportions among these three elements, significantly reducing the likelihood of by-products formation^[1d, 9]. Compared to the traditional binary-precursor hot-injection method, it is evident that the utilization rate for Pb and I-resource is greatly improved, thereby lowering the production cost to a certain extent and more suitable for commercial production. Additionally, increasing the iodine content in this preparation method created a halide-rich environment, which will greatly reduce surface vacancy defects, improves optical property and stability^[10]. However, PeLEDs based on these ternary-precursor method QDs show a brightness of only 365 cd/m², an EQE of 1.8%, and a half-lifetime (T₅₀) of 3.1 h^[10c]. While this represents a significant improvement in operational stability, the improvement of brightness and EQE remain limited. This is primarily attributed to the use of long-chain organic ligands like

oleylamine (OAm) and oleic acid (OA) during synthesis. While these ligands help passivate QDs and stabilize their cubic structure^[1k], their poor conductivity hinders charge transport. To better apply it in PeLEDs, partially attached OA and OAm ligands are tried to remove from the QDs surface, which leads some Pb or I vacancies defects to the originally nearly defect-free QDs again^[11]. Hence, this purification process can cause lattice damage, leading to a decrease in the overall performance of the QDs. Therefore, further optimization on integrality of surface and lattice is necessary. In recent years, GA salts has been widely employed as a superior additive to enhance the performance of PeLEDs and solar cells. Existing reports primarily attribute the optimization mechanism of GA salt to Cs⁺ substitution, halide vacancy passivation, and ligand exchange. For instance, Hinako et al. report a method for passivating surface vacancies in CsPbI₃ using a mixed solution of GA salt and methyl acetate^[12]. While GA can act as an effective surface ligand to enhance QDs stability, the use of the polar solvent methyl acetate may compromise the QDs to some extent. I Minh et al. dissolve GA salt in tetrahydrofuran (THF) and treated CsPbI₃ QDs^[13]. However, THF also result in QDs degradation. The PeLEDs based on these QDs showed a T₅₀ of only 20 min and an EQE of 13.8%. Therefore, maintaining the stability of QDs during ligand exchange in highly polar GA salt solutions remains challenging. Furthermore, Yao et al. introduce GA₂CO₃ into the PbI₂ precursor solution before injecting a Cs precursor solution^[2e]. GA⁺, acting as a surface ligand, efficiently passivates surface defects in the QDs, enhancing their optical properties and stability. However, the initial stoichiometric ratio of Pb/I resulted in a certain amount of iodine vacancies in the final QDs, which are further increased after purification process, ultimately limiting their luminescence properties. Patricio et al. introduce GAOAc during synthesis to partially replace Cs⁺, thereby enhancing stability and suppressing lattice distortion^[14]. However, further purification steps in the subsequent PeLEDs fabrication leads to a significant increase in surface vacancies, resulting in an EQE of only 19% and a T₅₀ of only 25 min. While both studies introduce GA salts to stabilise QDs properties, they are unable to prevent the degradation of QDs performance after purification. Besides, in current PeLEDs architectures, the surface phase transition of CsPbI₃ and structural collapse induced by I vacancy migration under an electric field are the primary causes of performance degradation, and also major limiting factors in the stress testing of PeLEDs^[15]. In general, intrinsic I vacancies in the CsPbI₃ QDs can act as the active sites for ion migration under bias voltage, and the surface vacancies defects on the α -CsPbI₃ QDs are easier to inducing lattice distortion in the Pb-I octahedron. In addition, such lattice distortion may lead to the decomposition of α -CsPbI₃ into γ -CsPbI₃ even as δ -CsPbI₃. This process could aggravate the significant loss of iodine heavily. Iodine deficiency can lead to an increased density of iodine vacancies, contributes to further performance degradation of PeLEDs. Therefore, minimizing surface iodine vacancies and enhancing sample stability are crucial aspects of the optimization process. The performance of PeLEDs arises from the synergistic effect of multiple parameters, addressing the limitations of previous work is crucial for further performance enhancement.

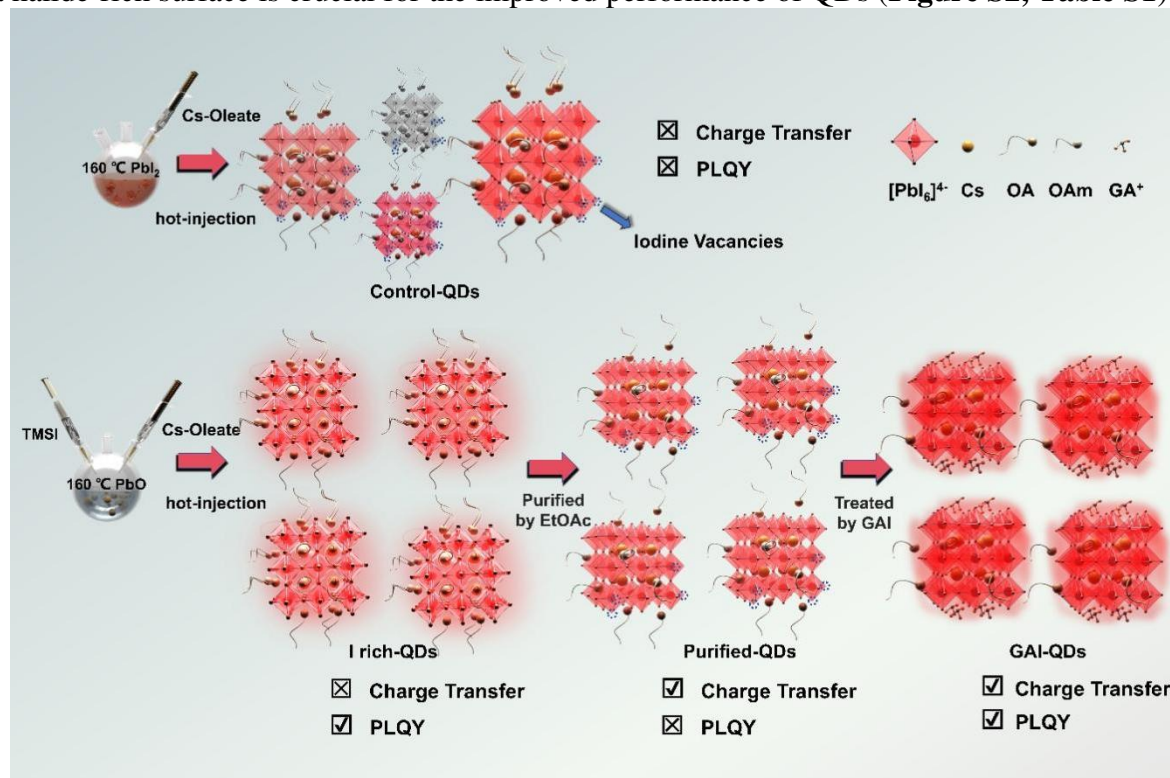
In order to results these limitations, we design a novel synthesis method based on synergistic effects of halide-rich modulation passivation and lattice repair. Firstly, we construct a halide-rich environment using a ternary-precursor method which can allow for flexible adjustment of feed ratio, improving the optical properties of the QDs. Furthermore, GA⁺ can act as a short-chain ligand with good conductivity, replacing the long-chain ligands of OAm and facilitating charge transport, significantly enhancing the performance of the fabricated PeLEDs. The resulting GAI-QDs exhibit a uniform size distribution, with an excellent stability, and a high PLQY of 97%. In addition, the resulting PeLEDs based on GAI-QDs show an excellent EQE of 27.1%, a maximum luminance of 3949 cd/m² and a T₅₀ of 1001.1 min with an initial luminance of 100 cd/m², which is nearly 1.9 times, 48.9 times and 19.2 times as high as that of PeLEDs based on control-QDs. This is primarily due to the reduction of trap states in the QDs after treatment with GAI, which inhibits intradot biexciton Auger recombination and trap-

assisted Auger recombination, reducing energy loss and retaining high EQE at high brightness. Additionally, GAI treatment also suppresses intradot biexciton Auger recombination, which reduce the heat accumulation during the operation of PeLEDs and enhance operational stability.

2. Results and Discussion

Typically, CsPbI₃ QDs are prepared by the binary-precursor hot-injection method (Control-QDs), where Cs₂CO₃ is used as cesium resource, PbI₂ is selected as lead and iodine sources, with a molar ratio of Cs/Pb/I in the reaction system of only 1/1/2. This ratio is significantly smaller than the stoichiometric ratio of 1/1/3. It is hard to form an I-rich surface structure which is beneficial to both high stability and PLQYs in this iodine-insufficient synthetic environment. Control-QDs exhibit high density of iodine vacancy defects on the surface, thereby resulting in the poor PLQY and stability^[16]. Therefore, to overcome these issues, a ternary-precursors method is devised, separately prepares the three precursors of cesium, lead and iodide and mixes them in a halide-rich environment at a specific temperature. In this study, I rich-QDs refer to the CsPbI₃ QDs prepared under a I-rich environment based on the ternary precursor method. OAm and OA are commonly used as capping ligands for surface passivation of QDs, but both ligands are insulating, which is unfavorable for the charges transport of the QDs, further purification process for the prepared QDs is needed (All preparation processes are shown in **Scheme 1**). This process leads to the iodide-insufficient QDs surface because of the labile binding of OAm and OA (called Purified-QDs), and the I⁻ ions on the surface tend to detach with the loss of long-chain ligands, thereby damaging the lattice structure, leading to the deterioration of the optical performance and stability of the QDs. Therefore, additional optimization treatment is devised to passivate the iodine vacancies defects and promote secondary growth for lattice surface repair. GAI is chosen for this purpose, where bigger GA⁺ ions partially replaced Cs⁺ ions to increase the tolerance factor as the calculation of the tolerance factor in **Supporting Information** shown, the tolerance factor of GAPbI₃ can reach approximately 1.5. Consequently, doping with GA⁺ ions can enhance the tolerance factor of CsPbI₃, while compensating for surface vacancy defects (**Scheme 1**, called GAI-QDs). In addition, GAI can be used as short-chain ligands, which is contributed to the carrier injection and transport. Hence, CsPbI₃ QDs with excellent optoelectronic properties and stability can be achieved based on synergistic effect. As is exhibited in **Figure 1a**, transmission electron microscopy (TEM) images of Control-QDs exhibit poor uniformity and widen size distribution of 14.6±5.3 nm. Moreover, there are numerous bright white spots present on the surface of the QDs. This can be owed to the high density of iodine vacancies on the QDs surface, which increases the sensitivity of the QDs to electron beams, leading to the reduction of surface-exposed Pb ions to elemental Pb^[17]. In comparison to Control-QDs, the I rich-QDs have a more uniform lattice size distribution of 13.8±2.3 nm with fewer exposed Pb atom, indicating fewer vacancy defects. It shows that iodide-rich environment can improve crystal quality of QDs. Additionally, many lattices in Control-QDs undergo distortion, significantly affecting their optical property, whereas I rich-QDs experience only minor lattice changes, resulting in less negative impact (**Figures S1 a, b, e, f**). It is indicated that lattice distortions arise from the I vacancies, but constructing halide-rich environment can efficiently suppress vacancies, alleviate lattice distortions. In addition, Control-QDs exhibit a PL emission at 683.7 nm with full width at half maximum (FWHM) of 45.4 nm, and an obvious absorption peak at 500 nm because of the generation of excessive by-products, while I rich-QDs show no such absorption peak in their absorption spectra, indicating the absence of by-products based on this iodide-rich method. I rich-QDs show a blue-shift PL emission peak at 682.5 nm with the narrower FWHM of 38.4 nm, corresponding to the TEM results. The PLQY also increases from 81% to 92% (**Figures 1 a-f**), indicating deceased iodides vacancies. However, after purification, PLQY of

Purified-QDs decrease from 92% to 84%, an obvious lattice distortion can be observed in **Figure S1**, and a new absorption peak at 500 nm emerges. It is owed to the loss iodide ions during the purification of I rich-QDs, which leads to a halide-deficiency surface, hinder their further applications of PeLEDs. After introduction of GAI, these surface defects can be efficiently repaired, resulting in the improved crystal quality and optical properties of GAI-QDs. **Figure 1g** and **Figure S1** show that the repaired GAI-QDs have no exposed Pb atoms on the surface and resolve lattice damage. Compared to other QDs, GAI-QDs exhibit a more uniform size distribution of 13.7 ± 1.5 nm, a PL emission peak at 682.1 nm with a further reduced FWHM of 37.8 nm and an increased PLQY of 97% (**Figures 1h, i**). Furthermore, as is shown in **Figures 1a, d, g**, the interplanar spacing of the three samples progressively increases. The Control-QDs exhibit the smallest interplanar spacing, attributed to lattice contraction resulting from the reduction of a significant proportion of surface ions to atoms. I rich-QDs exhibit a slightly increased interplanar spacing due to the filling of most vacancy defects. The increased interplanar spacing observed in GAI-QDs is primarily attributed to the expansion of lattice resulting from the substitution of some Cs^+ ions with larger GA^+ ions. Elemental analysis based on EDS mapping reveals a Cs/Pb/I ratio of 1:1.2:2.1 in Control-QDs, 1:1.1:3.4 in I rich-QDs, 1:1.2:2.9 in Purified-QDs and 1:1.1:3.2 in GAI-QDs. Notably, GAI-QDs exhibit a pronounced halide enrichment, consistent with their enhanced optical properties. This finding suggests that a halide-rich surface is crucial for the improved performance of QDs (**Figure S2, Table S1**).



Scheme 1. The schematic diagram of binary-precursor method and synergistic effect of halide-rich modulation and lattice repair.

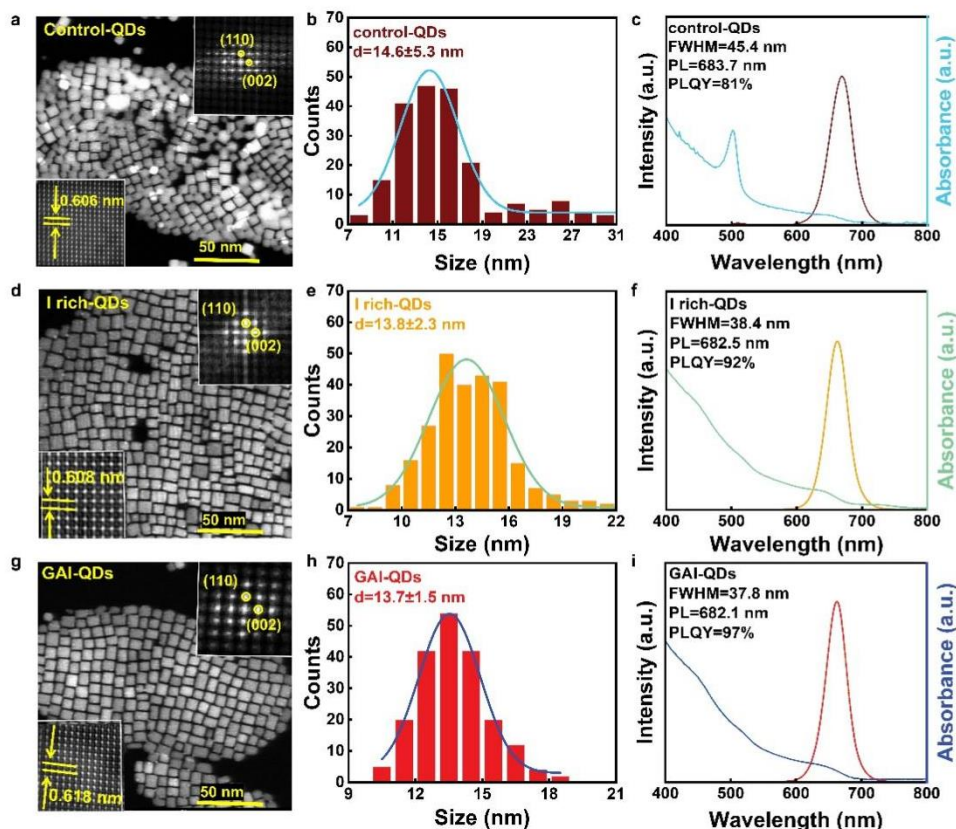


Figure 1. Morphology and optical performance of the QDs. TEM images of **a)** Control-QDs, **d)** I rich-QDs, **g)** GAI-QDs. The size distribution histograms of **b)** Control-QDs, **e)** I rich-QDs, **h)** GAI-QDs. The UV-visible absorption and PL spectra of **c)** Control-QDs, **f)** I rich-QDs, **i)** GAI-QDs.

One of the primary pathways for energy loss in QDs is the rapid cooling of hot charge carriers. Longer relaxation times provide a greater time window for hot electrons to collect energy before being scattered by phonons, resulting in enhanced energy harvesting^[18]. Therefore, the relaxation time of hot charge carriers is significant research in optical properties of QDs. To further compare the performance of the different QDs, the femtosecond transient absorption (TA) measurements are conducted (**Figure S3**). Comparative validation leads to the selection of 420 nm as the optimal excitation wavelength for TA measurements, with a detailed justification provides in the **Supporting Information** of **Figure S3**.

Figures 2a-c depict the TA spectra collected under 420 nm excitation for the different samples. A comparative analysis of the absorption spectra at different pump-probe delay time is conducted. Generally, TA spectra exhibit several common features above the bandgap of the excited semiconductor. These features include bandgap-induced absorption bleaching (PB1), high-energy side-induced absorption bleaching (PB2), and low-energy side-induced absorption (PA2)^[19]. The relaxation of hot excitons leads to the filling of states at the band edge, significantly enhancing PB1. When all the hot excitons relax to lower energy levels, PB1 reaches its maximum value, and PB2 disappears^[20]. Therefore, it can be approximated that a larger PB2 at the initial stage corresponds to a greater energy loss in the hot carrier relaxation process. Furthermore, rapid cooling of hot carriers is a main pathway resulting in energy loss. Therefore, a longer hot carrier relaxation time results in higher energy utilization efficiency^[21]. Due to the relatively large bandgap of CsPbI₃, the PB2 band is not prominently observed, and it only leads to some blue shift in PB1 band. Hence, both PB1 and PB2 are considered as a single PB peak here. For the GAI-QDs, the PB peak demonstrates only a 3 nm blue shift, while I rich-QDs exhibit a 5 nm blue shift. Purified-QDs show a 8 nm blue shift, whereas the Control-

QDs display a blue shift of 10 nm (**Figures 2d-f** and **Figure S4**). It can be inferred that the observed variation is primarily caused by the different energy losses in the hot carrier relaxation process, with GAI-QDs experiencing the least energy loss and Control-QDs experiencing the most. To validate this hypothesis, a further comparative analysis of the PB and PA2 peaks within the first 10 ps for the four samples is conducted. It is observed that Control-QDs exhibit the shortest relaxation time of only 0.2 ps, the relaxation time of I rich-QDs fabricated in a halogen-rich environment increases to 0.3 ps. However, purification of Purified-QDs resulted in a reduced surface ligand density and increased defect concentration, leading to a decrease in relaxation time (0.2 ps), while GAI-QDs, following optimization, exhibit the longest relaxation time (0.6 ps), significantly improving its energy utilization efficiency. Generally, the stronger carrier-phonon coupling effect (CPC), the faster cooling rate of hot carriers. However, in this case, the dimensions of these QDs exceed the Bohr radius of CsPbI₃, strong quantum confinement does not exist. The phonon mode of CsPbI₃ mainly concentrate on the PbI₂ framework. Vibrations of the A-site cations can couple with PbI₂, leading to non-adiabatic coupling that promotes relaxation processes. In general, the larger cations exhibit the stronger interactions with the PbI₂ framework, resulting in significantly reduced relaxation times and increased energy loss. In general, Cs itself has negligible contribution to the density of states (DOS) related to the conduction band and valence band^[22]. Therefore, the increased relaxation time of I rich-QDs prepared in a halide-rich environment is not related to the coupling between A-site cations and PbI₂. It is speculated that the halogen-rich environment suppresses iodine vacancies within the QDs, significantly enhancing the crystal quality of QDs, suppressing phonon coupling processes, thus increasing relaxation time^[23]. In the case of GAI-QDs, although GA is larger than Cs, which would seemingly promote relaxation process, the actual relaxation time of GAI-QDs is greater than that of I rich-QDs. This is attributed to the fact that GA is an organic A-site cation, which weakens the interaction between the organic cation and the PbI₂ framework. As a result, under the influence of GA, the relaxation process of hot carrier is effectively mitigated^[24]. Furthermore, GA⁺ acted as a surface ligands show a smaller steric hindrance compared to long-chain ligands OA and OAm, allowing for a higher ligand density on the QDs surface. It is also contributed to prolong relaxation process. To gain a detailed understanding of the carrier dynamics among the different QDs, the absorption signal bleaching recovery dynamics are normalized and fitted (**Figure 2h** and **Figure S4**). A comparison of the TA lifetime as is shown in **Table S2**. The fast component (τ_1) is attributed to the generation of Auger recombination and trap-assisted nonradiative recombination, while the slow component (τ_2) originates from the intrinsic edge exciton recombination of the QDs^[25]. It is evident that the non-radiative relaxation process is significantly suppressed in GAI-QDs, indicating fewer defects in the QDs. A detailed analysis of this process is presented in the **Supporting Information** of **Table S2**. Furthermore, a detailed analysis of the bleaching-recovery dynamic curves in both states is conducted for I rich-QDs and GAI-QDs, providing further comparison of their Auger recombination processes. For detailed information, refer to **Tables S3** and **S4**. To further demonstrate the impact of reduced defect density on the performance of QDs, we conduct an analysis by time-resolved photoluminescence (TRPL). As is exhibited in **Figure 2i** and **Table S5**, the average lifetime of Control-QDs is only 25.8 ns, I rich-QDs show a slight increase (29.3 ns), while GAI-QDs exhibit a significant enhancement to 70.3 ns. The radiative recombination ratio (f_1) of Control-QDs is 78.7%, while I rich-QDs (91.0%) and GAI-QDs (100%) show a significant increase in f_1 . The non-radiative recombination ratio (f_2) of Control-QDs is 21.3%, while I rich-QDs (9.0%) and GAI-QDs (0%) show a significant decrease in f_2 . Surface defects are widely recognized to have the ability to serve as non-radiative recombination centers, and a smaller non-radiative recombination coefficient indicates a lower trap density^[26]. Thus, the relatively high radiative to non-radiative recombination ratios in these samples indicate a reduced non-radiative recombination in GAI-QDs. Calculations based on their lifetimes and PLQY indicate a significant decrease in the non-radiative recombination rate

of I rich-QDs ($54.6 \times 10^{-13} \text{ s}^{-1}$) compared to Control-QDs ($128.1 \times 10^{-13} \text{ s}^{-1}$). This is primarily owed to the significant decrease in defect density within the QDs, which is a result of the halide-rich environment. Besides, the non-radiative recombination rate of GAI-QDs ($4.3 \times 10^{-13} \text{ s}^{-1}$) is significantly decreased compared with I rich-QDs and Control-QDs, further confirming the effective suppression of non-radiative recombination in GAI-QDs due to the halide-rich synthesis and lattice repair.

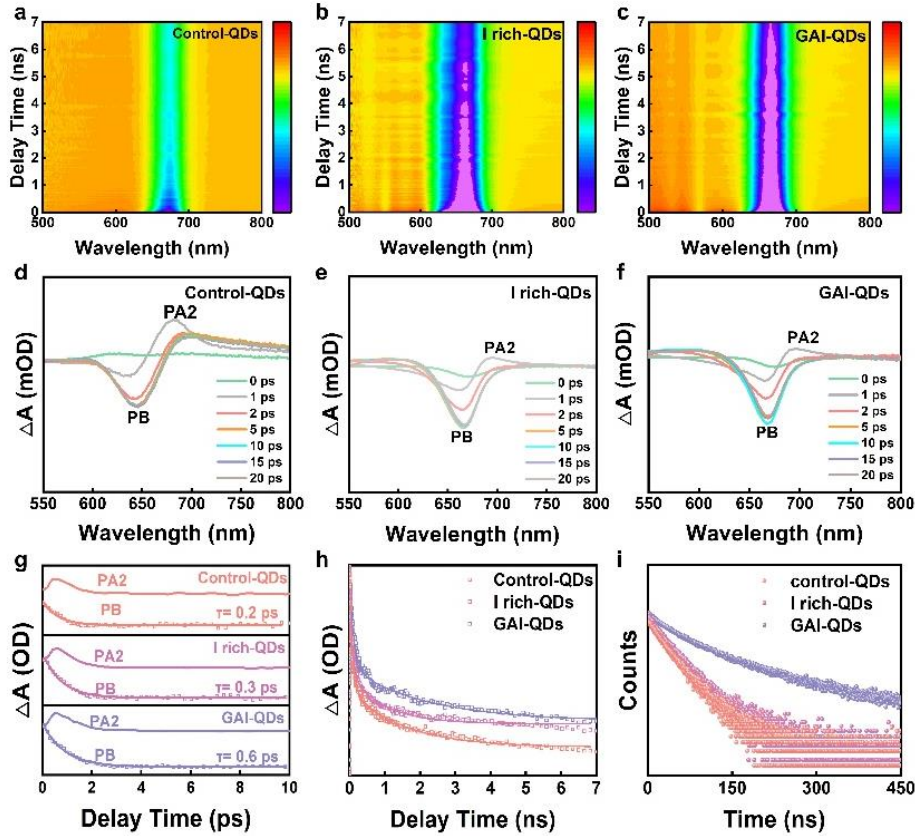


Figure 2. Exciton dynamics of the QDs. Pseudo color TA plot of **a)** Control-QDs, **b)** I rich-QDs, **c)** GAI-QDs. The TA spectra of **d)** Control-QDs, **e)** I rich-QDs, **f)** GAI-QDs at different delay times. **g)** The comparison of the formation and decay kinetics of PB and PA2 bands. **h)** TA bleach recovery curves, and **i)** time-resolved PL-decay transients of Control-QDs, I rich-QDs and GAI-QDs.

In addition to the impact of hot carrier relaxation time on device applications, Auger recombination phenomenon is also a common nonradiative recombination process for QDs. The electrical excitation of QDs typically involves high power densities, making it prone to Auger recombination during the operation of a PeLEDs, which leads to a roll-off of efficiency at high brightness. It is usually attributed to the accumulation of carriers inside QDs due to their high exciton binding energy (E_b). **Figures 3a, c** and **Figure S5** show the PL spectra of these QDs as a function of temperature. It is evident that the PL intensity shows a substantial decrease as the temperature rises. Additionally, the PL exhibits a blue shift with increasing temperature, primarily attributed to lattice expansion and electron-phonon interactions induced by temperature. At higher temperature, thermal activation energy enables low-energy carriers to jump and occupy higher energy levels of strongly localized states, causing some blue shift in peak energy^[27]. The lattice stability of QDs can be assessed based on the observed blue shift phenomenon. The blue shift trend with increasing temperature is significantly reduced for GAI-QDs, indicating their great lattice stability and a reduced tendency for low-energy carriers to transition to higher energy levels, leading to less thermal energy losses, which can contribute to a considerable enhancement to the performance of PeLEDs. According to this observation,

E_b for GAI-QDs (22.7 meV) is significantly lower compared to the E_b for I rich-QDs (40.0 meV) and Control-QDs (68.1 meV) (**Figures 3b, d** and **Figure S5**). We speculate that the introduction of GAI not only fills surface defects but significantly alters the charge distribution on the I rich-QDs surface, influencing the interaction between charge carriers and excitons, leading to a further decrease in E_b . This inference implies that the suppression of Auger recombination is a consequence of the reduced E_b . Due to the recognition of biexciton recombination as the primary Auger recombination process in QDs, a more detailed comparison of the Auger recombination in QDs is conducted. By utilizing the widely accepted universal proportionality relationship between biexciton lifetime and the volume of QDs for biexciton Auger recombination, we explore the biexciton recombination dynamics of these QDs samples.

To achieve this, we study the dynamic process of its variation by changing the pump intensity during the TA measurements. As is shown in **Figures 3e, g** and **Figure S5**, the decay processes at different pump intensities are clearly displayed. The decay of Control-QDs exhibits the fastest decay trend with increasing pump intensity, while the decay curves of I rich-QDs show the relatively slower decay rate than that of Control-QDs. This can be attributed to the suppressed trap-assisted Auger recombination in the I rich-QDs, which can be owed to the decreased trap states in I rich-QDs synthesized in a halide-rich environment. In contrast, the decay rate of GAI-QDs exhibits a significantly slowest decrease with increasing excitation power. With increasing excitation density, a fast decay component with a timescale of a few to tens of seconds appears, which is a typical feature of multiexciton recombination. Through measurements, the biexciton dynamics of these samples are obtained. By subtracting the biexciton dynamics, the corresponding single exciton lifetimes are obtained. As Control-QDs cannot be fitted with a single exponential even at low power, it can be inferred that their single-exciton lifetime is very short, indicating serious Auger recombination. The biexciton lifetime of GAI-QDs (287.9 ps) is much larger than that of I rich-QDs (191.5 ps), as is shown in **Figures 3f, h**, indicating a suppression of Auger recombination within GAI-QDs. This change is primarily owed to the strong coordination binding of GAI, which repairs the lattice and creates a surface-halide-rich environment. This significantly reduces the defect density in QDs, leading to a decrease in trap-assisted Auger recombination. In addition, GAI can act as ligands and effectively change the electron cloud distribution, alleviating carrier accumulation (**Figure S6**). A detailed analysis of this process is provided in the **Supporting Information** of **Figure S6**.

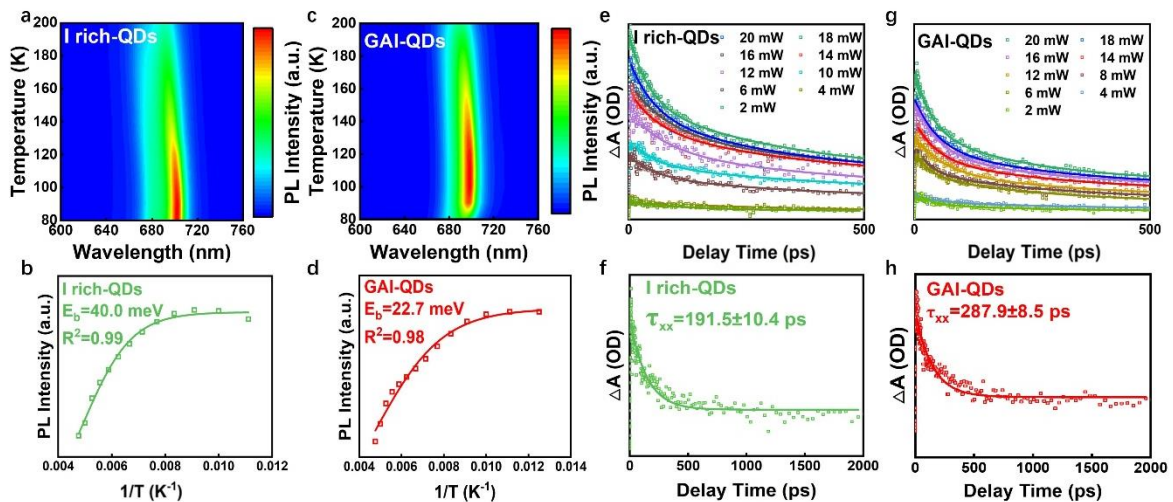


Figure 3. Auger recombination for QDs. Temperature-dependent spectra of **a)** I rich-QDs and **c)** GAI-QDs, integrated PL intensity for **b)** I rich-QDs and **d)** GAI-QDs. TA bleach recovery kinetics of **e)** I rich-QDs and **g)** GAI-QDs at different pulse energy density. Isolated decay curve of biexciton Auger recombination for the **f)** I rich-QDs and **h)** GAI-QDs.

The X-ray diffraction (XRD) measurements in **Figure 4a** show that all of the QDs, correspond well to the α -cubic phase without undergoing any phase transition, and no additional peaks appeared. It indicates that there are no by-products generated, and the original structural integrity is preserved without any damage, thus maintaining its various excellent optical properties^[13]. The X-ray photoelectron spectroscopy (XPS) research in **Figures 4b-d** reveals that compared to Control-QDs, the Pb 4f core level peaks of I rich-QDs and GAI-QDs, originally located at 137.7 eV and 142.6 eV, shift to higher binding energy. It indicates a low density of iodide vacancies around the surface of QDs and an improvement in the coordination of surface Pb²⁺ ions, with GAI-QDs exhibiting the best coordination^[12]. This conclusion can be further verified by contrasting the Urbach energy (E_u) values of the three QDs (**Figure S7**), as detailed in the **Supporting Information** of **Figure S7**. In addition, **Figure S8** shows a comparative XPS analysis of I rich-QDs, the surface/interior of purified QDs, GAI-QDs confirming that the lattice distortion in this work primarily originates from the QDs surface, as detailed in the **Supporting Information** of **Figure S8**.

For the N 1s level analysis, only one peak corresponding to the NH₃ group of OAm is observed at 401.7 eV in I rich-QDs and Control-QDs. However, an additional peak at 400 eV corresponding to the -NH₂ group can be observed for the GAI-QDs, which is attributed to the introduction of GA⁺, confirming that the surface of CsPbI₃ retains some GA⁺. This provides strong evidence that, GAI fulfills a double role on the surface of the QDs, as it not only fills surface iodine vacancies with iodide ions, GA⁺ but also serves as a ligand. The increased ligand density significantly enhances the overall lattice vibration resistance of the QDs, thus effectively suppressing the relaxation process. In addition, GAI-QDs shows some shift to the low binding energy of Cs 3d compares to I rich-QDs. This phenomenon is primarily owed to some substitution of Cs⁺ ions with GA⁺ ions within the lattice of CsPbI₃, resulting in competitive coordination of Cs⁺ and GA⁺ with I ions. The interactions between the QDs surface and the ligand species are efficiently detected through Fourier transform infrared (FTIR) spectra. As is depicted in **Figure 4e**, a signal peak representing the C=N bond emerges in FTIR spectra of GAI-QDs compared with I rich-QDs and Control-QDs, confirming the attachment of GA to the QDs surface. Additionally, a broad peak at ≈ 3120 cm⁻¹ stands for the NH₃ stretching mode of OAm. The intensity of this peak decreases after GA treatment, indicating that moderate GAI treatment can remove some long-chain OAm ligands from CsPbI₃ QDs and replace them with short-chain GA ligands, significantly improving their conductivity without compromising stability. The crucial role of GA⁺ in reducing the surface defect density of CsPbI₃ is elucidated through Density Functional Theory (DFT) calculations. We select the surface enriched with PbI₂ of CsPbI₃ as the termination surface and exposed lattice plane (001). Firstly, the adsorption energies (E_{abs}) of OAm, OA and GA⁺ on the QDs surface are compared (**Figure 4f**). The E_{abs} values for OAm, OA, and GA⁺ on the (001) plane are 0.9 eV, 0.5 eV, and 1.7 eV. It can be seen that GA has stronger surface-ligand interactions and is more likely to replace the surface OAm ligands. Furthermore, GAI can passivate QDs more effectively than OAm, leading to enhanced PLQY and stability, consistent with the results of transient and steady-state spectra mentioned before. Iodine vacancies on CsPbI₃ surfaces is considered the main defect of QDs. We compare the formation energy (E_f) values of CsPbI₃ capped with OAm/OA and CsPbI₃ capped with GA/OA ligand pair. The E_f values for CsPbI₃ surfaces capped with ligand pair OAm/OA and GA/OA are determined to be 2.8 eV and 3.3 eV, separately (**Figure 4g**). It is evident that the E_f value of GAI-QDs increases, indicating increased difficulty in forming iodine vacancy defects. Additionally, testing for environmental stability, fluorescence stability and the change of XRD (**Figures S9, S10**) clearly reveals that Control-QDs exhibit the poorest stability, while GAI-QDs exhibit best stability compared to the other two samples. This is primarily attributed to the inherent presence of a high density of iodine vacancy defects in Control-QDs, which while inducing lattice distortion, leading to a significant decrease in stability. Although I rich-QDs are prepared in a halide-rich environment, which significantly enhances their stability,

both OAm and OA on the surface are prone to detachment with surface atoms, which can affect the stability of I rich-QDs. In contrast, the further processing of GAI-QDs effectively passivates surface vacancy defects and GA^+ binds firmly to the surface of GAI-QDs while repairing and suppressing lattice distortion, resulting in a substantial enhancement of their stability. In addition, a comprehensive explanatory analysis of the differences in charge density resulting from the interaction between various ligands and the QDs surface, as well as the data on the DOS, which has been provided in the **Supporting Information of Figures S11**.

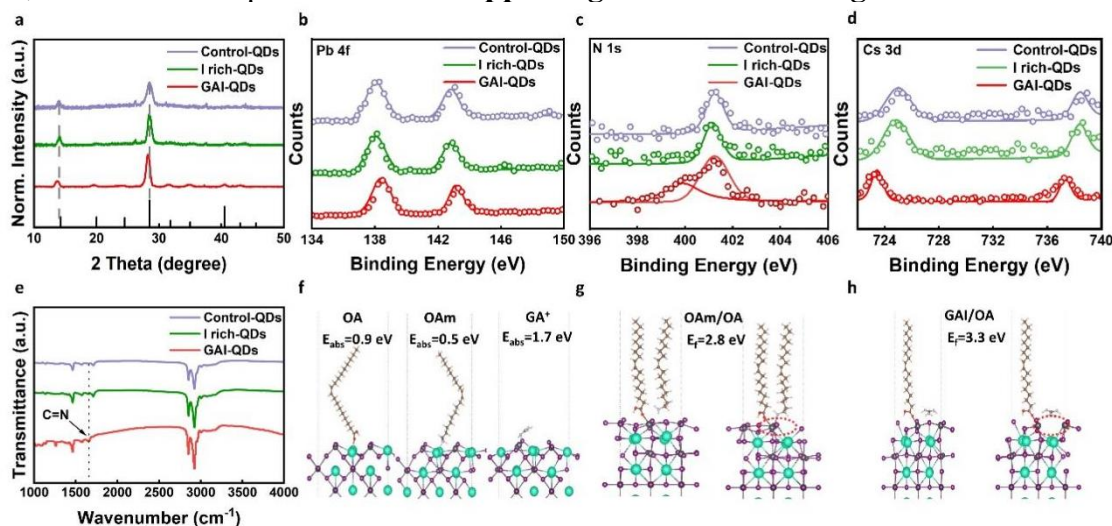


Figure 4. The surface ligand situation of QDs. a) Comparison of XRD of the Control-QDs, I rich-QDs and GAI-QDs. XPS survey spectrum of Control-QDs, I rich-QDs and GAI-QDs. b) Pb-4f spectrum, c) N-3d spectrum, d) Cs-3d spectrum. e) FTIR spectra results for Control-QDs, I rich-QDs and GAI-QDs. f) The DFT calculations of the adsorption energies of ligands (OA and OAm) on the surface of GAI-QDs. The DFT calculations of iodine defective formation energy of g) I rich-QDs capped with OAm/OA ligand pair, h) GAI-QDs capped with GA/OA.

As is shown in **Figure 5a** we fabricate PeLEDs with the structure of polystyrenesulfonate (PEDOT:PSS)/poly (N,N'-bis (3-methylphenyl)-N,N'diphenyl-benzidine) (poly-TPD)/CsPbI₃ QDs/2,2',2''-(1,3,5-benzinetriyl)-tris(1-phenyl-1-H-benzimidazole) (TPBi)/LiF/Al. As is exhibited in **Figure S12**, PeLEDs based on Control-QDs show an EL emission peak at 683 nm with the FWHM of 38.3 nm. Conversely, the PeLEDs based on I rich-QDs show an EL emission peak at 685 nm with the FWHM of 38 nm, the PeLEDs based on GAI-QDs show a narrower EL emission peak at 683 nm with the FWHM of 37.5 nm (**Figure 5b**). This can be primarily attributed to the uniform size distribution and fewer defects present in TE and GAI-QDs, which is totally in line with the results of TEM and PL spectra. **Figures 5c and S12** depict the current density-voltage-luminance (J-V-L) curves of the PeLEDs. The PeLEDs based on Control-QDs exhibits a highest turn-on voltage (2.5 V), which significantly limits its operational capability. In comparison to the PeLEDs based on I rich-QDs (1.9 V), the PeLEDs based on GAI-QDs turns on at 1.75 V. Furthermore, at the same voltage, the PeLEDs based on GAI-QDs (3949 cd/m²) achieves a higher maximum luminance than the PeLEDs based on I rich-QDs (635.6 cd/m²), while the PeLEDs based on Control-QDs only reaches a luminance of 80.7 cd/m². This prominent improvement can be attributed to the diminished trap state density, extended thermal carrier relaxation time, and elevated carrier mobility of GAI-QDs. As **Figure 5d** and the data in **Figure S12** shown, the PeLEDs based on GAI-QDs show a best maximum EQE of 27.1%, which is much greater than the maximum EQE of PeLEDs based on I rich-QDs (15.4%) and Control-QDs (14.1%). It is attributed to the ultralow trap density and excellent carrier injection and transport of GAI-QDs, indicating that synergistic effect can effectively improve quality of

QDs. **Figure 5e** shows that the average peak EQE (averaged over 30 devices) of the PeLEDs based on GAI-QDs (24.7%) is much higher than that of the PeLEDs based on I rich-QDs (14.8%), indicating good reproducibility of device performance using GAI-QDs. Compared to the other two PeLEDs, PeLEDs based on GAI-QDs exhibit superior EL spectral stability (**Figure S13**). Previous studies have shown that I vacancies can act as sites for ion migration, exacerbating the migration of halide ions in QDs under an electric field, leading to a significant decrease for PeLEDs stability. Therefore, the reduced defect state density in GAI-QDs effectively minimizes the pathways for ion migration. Additionally, stability testing is conducted under a constant current density. The PeLEDs based on GAI-QDs achieve a T_{50} value of 1001.1 min at the initial brightness of 100 cd/m^2 (**Figure 5f**). This value is nearly 19.2 times as high as the T_{50} of the PeLEDs based on Control-QDs ($T_{50} = 52.2 \text{ min}$) and 6.5 times as high as the T_{50} of the PeLEDs based on I rich-QDs ($T_{50} = 154.1 \text{ min}$). Our PeLEDs shows an excellent combination property (EQE, luminance, spectral and operational stability) among reported state-of-art CsPbI₃ QDs LEDs (**Table S6**). At high luminance, the PeLEDs based on GAI-QDs exhibit a significantly lower efficiency roll-off compared to the PeLEDs based on I rich-QDs. Besides, as is shown in **Figure S15**, operating continuously for 10 min under room temperature and a working voltage of 5 V, the temperature of the PeLEDs based on Control-QDs reach 31.3 °C, the PeLEDs based on I rich-QDs exhibit a slightly lower temperature of 28.6 °C, while the PeLEDs based on GAI-QDs show a lowest temperature of only 19.5 °C. For PeLEDs, the length of the surface ligands on the QDs, defect density, and Auger recombination all contribute to device heating. In comparison with PeLEDs based on Control-QDs, the temperature of PeLEDs based on I rich-QDs shows a slight decrease, primarily attribute to the reduced defect density in the I rich-QDs. However, this decrease is only 2.5 °C, indicating that a reduction in defect density alone is insufficient to effectively relief PeLEDs heating. In comparison with PeLEDs based on I rich-QDs, the temperature of PeLEDs based on GAI-QDs is reduced to 19.5 °C. This is mainly because the introduction of GAI in GAI-QDs significantly inhibits phonon coupling compared to I rich-QDs, reducing the thermal loss caused by intradot biexciton Auger recombination. Additionally, GAI passivates surface defects, minimizing the generation of trap-assisted Auger recombination. Comparative analysis clearly demonstrates that Auger recombination exerts a significantly greater influence on the operating temperature of PeLEDs. A more detailed analysis of this process is provided in the **Supporting Information of Figure S15**.

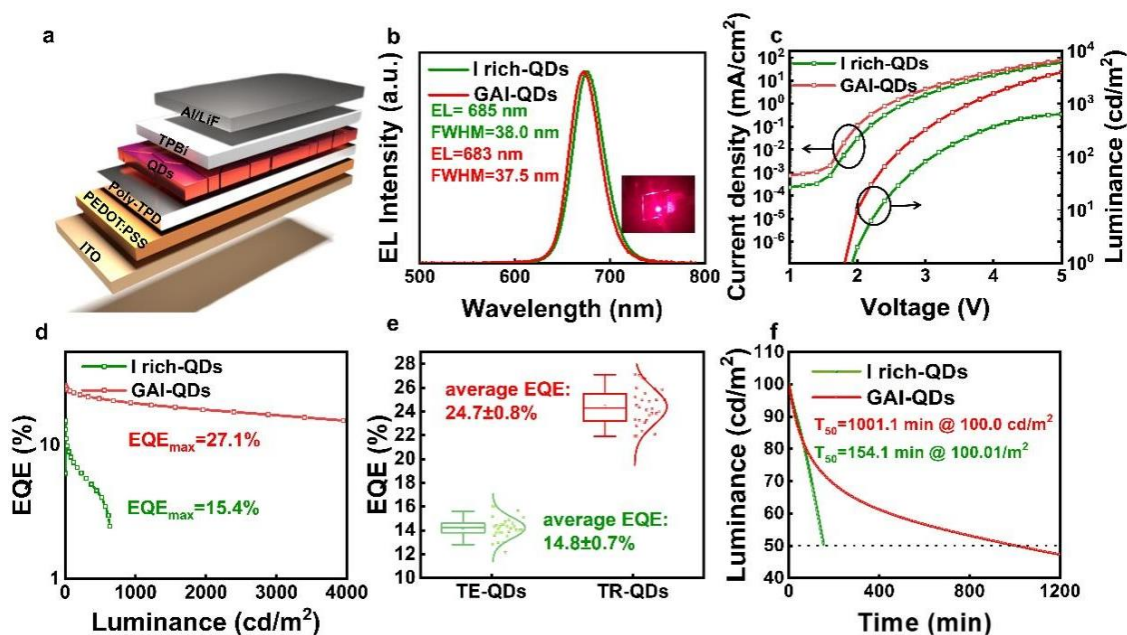


Figure 5. The performance of the PeLEDs based on the QDs. **a)** Schematic diagram of the PeLEDs device structure. **b)** EL spectra of PeLEDs based on I rich-QDs and GAI-QDs. **c)** J-V-L curves of PeLEDs based on I rich-QDs and GAI-QDs. **d)** EQE-L curves of PeLEDs based on I rich-QDs and GAI-QDs. **e)** The comparison of the average peak EQE of PeLEDs based on I rich-QDs and GAI-QDs. **f)** T_{50} of PeLEDs based on I rich-QDs at the initial luminance of 100 cd/m^2 and GAI-QDs at an initial luminance of 100 cd/m^2 .

3. Conclusion

In conclusion, we propose an efficient method to prepare CsPbI_3 QDs with excellent optoelectronic performance and surface stability based on a synergistic effect of halide-rich modulation and lattice repair. Firstly, we design ternary-precursor method to construct a halide-rich reaction environment and address the limitations of the traditional binary-precursor method. It has been showed that the molar ratio of Cs/Pb/I can be modified with flexibility in the reaction system, allowing for an optimized ratio that ensures high stability and performance of QDs. We then introduce multifunctional GAI additive based on solvent-free solid-liquid reaction post-treatment process to repair the damage of lattice caused by the purification process and maximizes the utilization of cations to achieve high-quality CsPbI_3 QDs. DFT calculation indicate that GA^+ exhibit a higher binding energy with QDs than that of OA and OAm. As a result, GA^+ can bind to the QDs surface as short-chain ligand, which can fully passivate surface trap states and increase carriers' mobility. In addition, ultrafast spectra reveal that GAI can also significantly suppress trap-assisted Auger recombination. The optical and electrical performances of QDs can be further enhanced, resulting in LEDs based on GAI-QDs exhibiting a promoted combination performance and stability. These LEDs achieve the EQE of 27.1% (the highest EQE compared to other reported CsPbI_3 QDs-based PeLEDs devices with red emission), a T_{50} of 1001.1 min with an initial luminance of 100 cd/m^2 , and maximum luminance of 3949 cd/m^2 . This approach provides valuable insights for large-scale production.

Supporting Information

Supporting Information is available from the Wiley Online Library or from the author.

Acknowledgements

This work was financially supported by the National Natural Science Foundation of China (No. 52302171), Shandong Provincial Natural Science Foundation, China (ZR2023QF005), Heilongjiang Provincial Natural Science Foundation of China (LH2023F026, LH2020A007 and LH2020F027), New Era Longjiang Excellent Doctoral Dissertation Project (LJYXL2022-003), Youth Innovation and Technology Support Program for colleges of Shandong Province (2024KJH050) and the Fundamental Research Funds for the Central Universities (3072024XX2606, 3072022TS2613, 79000012/012), Teaching Reform Research Project of Harbin Engineering University (79005023/013).

Author Contributions

†C.Y.G., and †C.H.B. contributed equally to this work and should be considered as co-first authors. C.Y.G. and C.H.B. initiated and designed the study. C.Y.G., S.B.W., K.R., L.T, X.X.H and J.C.H. performed experiments and analyzed data. C.H.B. and C.Y.G. performed PeLEDs devices and tested them. N.H.L. and X.Y.W. performed and interpreted the theoretical calculations. C.Y.G. performed the part of optical measurements. C.H.B. and W.X.W. guided the projects and revised the paper.

Conflict of Interest

The authors declare no competing financial interest.

Received: ((will be filled in by the editorial staff))

Revised: ((will be filled in by the editorial staff))

Published online: ((will be filled in by the editorial staff))

References

- [1] a)A. Swarnkar, A. R. Marshall, E. M. Sanehira, B. D. Chernomordik, D. T. Moore, J. A. Christians, T. Chakrabarti, J. M. Luther, *Science* **2016**, 354, 92; b)Y. Hassan, J. H. Park, M. L. Crawford, A. Sadhanala, J. Lee, J. C. Sadighian, E. Mosconi, R. Shivanna, E. Radicchi, M. Jeong, *Nature* **2021**, 591, 72; c)X. Zhao, T. Liu, Q. C. Burlingame, T. Liu, R. Holley III, G. Cheng, N. Yao, F. Gao, Y. L. Loo, *Science* **2022**, 377, 307; d)Y. Wang, M. I. Dar, L. K. Ono, T. Zhang, M. Kan, Y. Li, L. Zhang, X. Wang, Y. Yang, X. Gao, *Science* **2019**, 365, 591; e)S. S. Mali, J. V. Patil, J. Shao, Y. Zhong, S. R. Rondiya, N. Y. Dzade, C. Hong, *Nat. Energy* **2023**, 8, 989; f)Y. Li, M. Deng, X. Zhang, T. Xu, X. Wang, Z. Yao, Q. Wang, L. Qian, C. Xiang, *Nat. Commun.* **2024**, 15, 5696; g)Y. Han, W. Liang, X. Lin, Y. Li, F. Sun, F. Zhang, P. C. Sercel, K. Wu, *Nat. Mater.* **2022**, 21, 1282; h)Y. Wang, T. Zhang, M. Kan, Y. Li, T. Wang, Y. Zhao, *Joule* **2018**, 2, 2065; i)J. Song, J. Li, X. Li, L. Xu, Y. Dong, H. Zeng, *Adv. Mater.* **2015**, 27, 7162; j)C. Bi, J. Hu, Z. Yao, Y. Lu, D. Binks, M. Sui, J. Tian, *Adv. Funct. Mater.* **2020**, 30, 2005990; k)L. Protesescu, S. Yakunin, M. I. Bodnarchuk, F. Krieg, R. Caputo, C. H. Hendon, R. Yang, A. Walsh, M. V. Kovalenko, *Nano Lett.* **2015**, 15, 3692; l) S. Mokkalapati, C. Jagadish, *Mater. Today* **2009**, 12, 22.
- [2] a)Y. H. Kim, J. Park, S. Kim, J. S. Kim, H. Xu, S. H. Jeong, B. Hu, T. W. Lee, *Nat. Nanotechnol.* **2022**, 17, 590; b) R. Wang, H. Xiang, H. Zeng, *J. Inorg. Mater.* **2023**, 38, 1062; c)J. Guo, Y. Fu, W. Zheng, M. Xie, Y. Huang, Z. Miao, C. Han, W. Yin, J. Zhang, X. Yang, *Nano Lett.* **2023**, 24, 417; d)W. Dong, H. Li, J. Li, Y. Hua, F. Yang, Q. Dong, X. Zhang, W. Zheng, *Nano Lett.* **2024**, 24, 3952; e)Y. Shi, L. Yuan, Z. Liu, Y. Lu, B. Yuan,

- W. Shen, B. Xue, Y. Zhang, Y. Qian, F. Li, X. Zhang, Y. Liu, Y. Wang, L. Wang, J. Yuan, L. Liao, B. Yang, Y. Yu, W. Ma, *ACS Nano* **2022**, 16, 10534.
- [3] a)S. Masi, A. F. Gualdrón-Reyes, I. Mora-Sero, *ACS Energy Lett.* **2020**, 5, 1974; b)J. A. Steele, H. Jin, I. Dovgaliuk, R. F. Berger, T. Braeckvelt, H. Yuan, C. Martin, E. Solano, K. Lejaeghere, S. M. Rogge, *Science* **2019**, 365, 679; c)F. Ke, C. Wang, C. Jia, N. R. Wolf, J. Yan, S. Niu, T. P. Devereaux, H. I. Karunadasa, W. Mao, Y. Lin, *Nat. Commun.* **2021**, 12, 461.
- [4] a)A. Swarnkar, W. J. Mir, A. Nag, *ACS Energy Lett.* **2018**, 3, 286; b)H. Zhao, J. Xu, S. Zhou, Z. Li, B. Zhang, X. Xia, X. Liu, S. Dai, J. Yao, *Adv. Funct. Mater.* **2019**, 29, 1808986.
- [5] a)F. Liu, C. Ding, Y. Zhang, T. Kamisaka, Q. Zhao, J. M. Luther, T. Toyoda, S. Hayase, T. Minemoto, K. Yoshino, *Chem. Mater.* **2019**, 31, 798; b)I. Lignos, S. Stavrakis, G. Nedelcu, L. Protesescu, A. J. Demello, M. V. Kovalenko, *Nano Lett.* **2016**, 16, 1869.
- [6] J. Jiang, S. Zhang, Q. Shan, L. Yang, J. Ren, Y. Wang, S. Jeon, H. Xiang, H. Zeng, *Adv. Mater.* **2024**, 36, 2304772.
- [7] X. Shen, Y. Zhang, S. V. Kershaw, T. Li, C. Wang, X. Zhang, W. Wang, D. Li, Y. Wang, M. Lu, *Nano Lett.* **2019**, 19, 1552.
- [8] J. Hu, C. Bi, K. Ren, X. Zhang, W. Wang, S. Ma, M. Wei, Y. Lu, M. Sui, *Nano Lett.* **2024**, 24, 4571.
- [9] B. Li, Y. Zhang, L. Fu, T. Yu, S. Zhou, L. Zhang, L. Yin, *Nat. Commun.* **2018**, 9, 1076.
- [10] a)M. Imran, V. Caligiuri, M. Wang, L. Goldoni, M. Prato, R. Krahn, L. De Trizio, L. Manna, *J. Am. Chem. Soc.* **2018**, 140, 2656; b)A. Dutta, R. K. Behera, P. Pal, S. Baitalik, N. Pradhan, *Angew. Chem. Int. Ed.* **2019**, 58, 5552; c)Y. Cai, H. Wang, Y. Li, L. Wang, Y. Lv, X. Yang, R. Xie, *Chem. Mater.* **2019**, 31, 881.
- [11] a)F. Liu, Y. Zhang, C. Ding, S. Kobayashi, T. Izuishi, N. Nakazawa, T. Toyoda, T. Ohta, S. Hayase, T. Minemoto, *ACS Nano* **2017**, 11, 10373; b)X. Zhang, M. Lu, Y. Zhang, H. Wu, X. Shen, W. Zhang, W. Zheng, V. L. Colvin, W. Yu, *ACS Cent. Sci.* **2018**, 4, 1352.
- [12] H. Ebe, R. Suzuki, S. Sumikoshi, M. Uwano, R. Moriyama, D. Yokota, M. Otaki, K. Enomoto, T. Oto, T. Chiba, J. Kido, *Chem. Eng. J.* **2023**, 471, 144578.
- [13] M. T. Hoang, A. S. Pannu, Y. Yang, S. Madani, P. Shaw, P. Sonar, T. Tesfamichael, H. Wang, *Nano-Micro Lett.* **2022**, 14, 69.
- [14] P. Serafini, A. Villanueva-Antolí, S. D. Adhikari, S. Masi, R. S. Sánchez, J. Rodriguez-Pereira, B. Pradhan, J. Hofkens, A. F. Gualdrón-Reyes, I. Mora-Sero, *Chem. Mater.* **2023**, 35, 3998.
- [15] J. Hu, C. Bi, X. Zhang, B. Tian, Y. Lu, J. Tian, M. Sui, *Appl. Surf. Sci.* **2023**, 626, 157289.
- [16] J. Xue, R. Wang, Y. Yang, *Nat. Rev. Mater.* **2020**, 5, 809.
- [17] X. Li, L. Teng, Y. Ren, R. Liu, X. Zhan, H. Sun, W. Zhang, J. Ding, H. Zhu, *ACS Appl. Mater. Interfaces* **2024**, 16, 43869.
- [18] a)M. Li, J. Fu, Q. Xu, T. C. Sum, *Adv. Mater.* **2019**, 31, 1802486; b)M. Li, S. Bhaumik, T. W. Goh, M. S. Kumar, N. Yantara, M. Grätzel, S. Mhaisalkar, N. Mathews, T. C. Sum, *Nat. Commun.* **2017**, 8, 14350.
- [19] N. S. Makarov, S. Guo, O. Isaienko, W. Liu, I. Robel, V. I. Klimov, *Nano Lett.* **2016**, 16, 2349.
- [20] N. Mondal, A. Samanta, *Nanoscale* **2017**, 9, 1878.
- [21] J. Butkus, P. Vashishtha, K. Chen, J. K. Gallaher, S. K. Prasad, D. Z. Metin, G. Laifersky, N. Gaston, J. E. Halpert, J. M. Hodgkiss, *Chem. Mater.* **2017**, 29, 3644.
- [22] B. Han, B. Cai, Q. Shan, J. Song, J. Li, F. Zhang, J. Chen, T. Fang, Q. Ji, X. Xu, *Adv. Funct. Mater.* **2018**, 28, 1804285.
- [23] a)J. Yang, X. Wen, H. Xia, R. Sheng, Q. Ma, J. Kim, P. Tapping, T. Harada, T. W. Kee, F. Huang, *Nat. Commun.* **2017**, 8, 14120; b)H. Shi, X. Zhang, X. Sun, X. Zhang,

- Nanoscale* **2018**, 10, 9892; c)A. Perumal, S. Shendre, M. Li, Y. K. E. Tay, V. K. Sharma, S. Chen, Z. Wei, Q. Liu, Y. Gao, P. J. S. Buenconsejo, *Sci. Rep.* **2016**, 6, 36733.
- [24] J. Chen, M. E. Messing, K. Zheng, T. Pullerits, *J. Am. Chem. Soc.* **2019**, 141, 3532.
- [25] S. Wei, J. Hu, C. Bi, K. Ren, X. Wang, N. H. de de Leeuw, Y. Lu, M. Sui, W. Wang, *Small* **2024**, 20, 2400885.
- [26] K. Ren, J. Hu, C. Bi, S. Wei, X. Wang, N. H. de de Leeuw, Y. Lu, M. Sui, W. Wang, *ACS Mater. Lett.* **2024**, 6, 4115.
- [27] a)A. Francisco-López, B. Charles, O. J. Weber, M. I. Alonso, M. Garriga, M. Campoy-Quiles, M. T. Weller, A. R. Goñi, *J. Phys. Chem. Lett.* **2019**, 10, 2971; b)P. C. Sercel, J. L. Lyons, D. Wickramaratne, R. Vaxenburg, N. Bernstein, A. L. Efros, *Nano Lett.* **2019**, 19, 4068.

Perovskite light-emitting diodes based on CsPbI₃ QDs obtained by synergistic effect of halide-rich modulation and lattice repair, exhibit the narrow deep-red emission (EL peak at 683 nm and FWHM of 37.5 nm) with luminance of 3949 cd/m², external quantum efficiency (EQE) of 27.1% and long-term operational stability (T₅₀) of 1001.1 min at 100 cd/m².

Keywords: perovskite quantum dots, halide-rich environment, lattice repair, PeLEDs, stability

Highly Efficient and Stable CsPbI₃ Perovskite Quantum Dots Light-Emitting Diodes through Synergistic Effect of Halide-rich Modulation and Lattice Repair

Chiyu Guo[†], Chenghao Bi^{†*}, Shibo Wei, Ke Ren, Xuexuan Huang, Liang Tao, Xingyu Wang, Nora H. de Leeuw, Wenxin Wang*

